LLNL-TR-686459

LAWRENCE
LIVERMORE
NATIONAL
LABORATORY

Polarimetric ISAR: Simulation and image reconstruction

D. H. Chambers

March 21, 2016

Disclaimer

This work performed under the auspices of the U.S. Department of Energy by Lawrence Livermore National Laboratory under Contract DE-AC52-07NA27344.

Polarimetric ISAR: Simulation and image reconstruction

David H. Chambers
Lawrence Livermore National Laboratory

February 29, 2016

1 Introduction

In polarimetric ISAR the illumination platform, typically airborne, carries a pair of antennas that are directed toward a fixed point on the surface as the platform moves. During platform motion, the antennas maintain their gaze on the point, creating an effective aperture for imaging any targets near that point. The interaction between the transmitted fields and targets (*e.g.* ships) is complicated since the targets are typically many wavelengths in size. Calculation of the field scattered from the target typically requires solving Maxwell's equations on a large three-dimensional numerical grid. This is prohibitive to use in any real-world imaging algorithm, so the scattering process is typically simplified by assuming the target consists of a cloud of independent, non-interacting, scattering points (centers). Imaging algorithms based on this scattering model perform well in many applications. Since polarimetric radar is not very common, the scattering model is often derived for a scalar field (single polarization) where the individual scatterers are assumed to be small spheres. However, when polarization is important, we must generalize the model to explicitly account for the vector nature of the electromagnetic fields and its interaction with objects. In this note, we present a scattering model that explicitly includes the vector nature of the fields but retains the assumption that the individual scatterers are small. The response of the scatterers is described by electric and magnetic dipole moments induced by the incident fields. We show that the received voltages in the antennas are linearly related to the transmitting currents through a scattering impedance matrix that depends on the overall geometry of the problem and the nature of the scatterers.

2 Simulated data

The basic problem for simulating ISAR data is to calculate the polarimetric response from a single scattering point S that is fixed to a ship near the origin point O (see Fig. 1). We transform to a coordinate system where the antennas are fixed and the platform motion becomes an effective motion of the ship. We assume the antennas are a pair of short crossed dipoles with one dipole (H) parallel to the ground (xz plane) and the other dipole (V) perpendicular to H but directly slightly downward toward point O. Let d_H and d_V be the lengths of the H and V dipoles respectively, then we can write the dipole vectors for each antenna as $\mathbf{d}_H = d_H(1,0,0)$ and $\mathbf{d}_V = d_V(0,\cos\theta_i,\sin\theta_i)$. For a scatterer S at $\mathbf{r} = (x,y,z)$ and antenna platform at $\mathbf{r}_a = (0,h,-z_a)$, the magnetic and electric fields at S are given by

$$\begin{aligned}\mathbf{H}_i &= \frac{ike^{ikR_S}}{4\pi R_s}\left[\hat{\mathbf{R}}_S \times (I_H\mathbf{d}_H + I_V\mathbf{d}_V)\right] \ , \\ \mathbf{E}_i &= -\frac{1}{\epsilon_0 c}\hat{\mathbf{R}}_S \times \mathbf{H}_i \ . \end{aligned} \tag{1}$$

I_H and I_V are the currents in each dipole, ϵ_0 is the permittivity of free space, $k = 2\pi f/c$ is the wave number at frequency f, c is the speed of light, and $\hat{\mathbf{R}}_S = \mathbf{R}_S/R_S$ is the unit vector between the scatterer and the antennas (R_S is the separation distance).

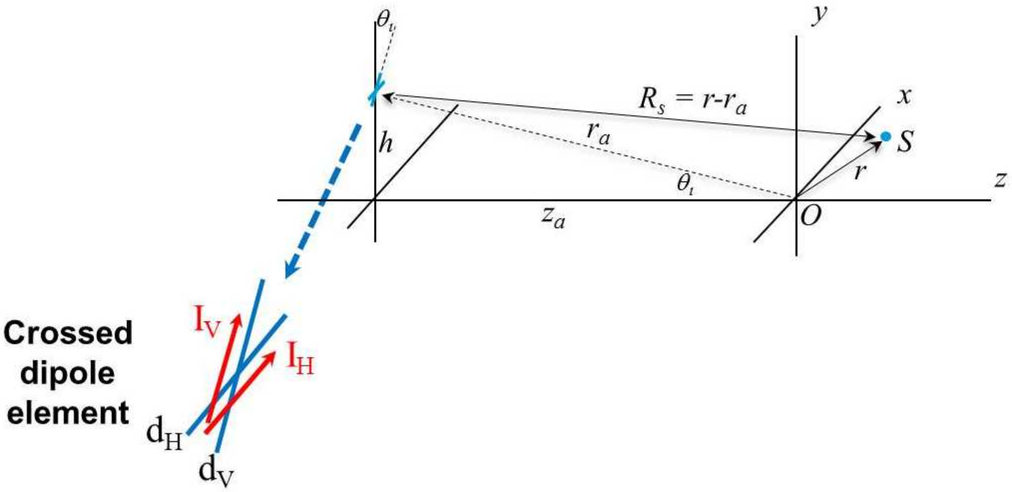

Figure 1: ISAR geometry for calculating the reflection from a point scatterer S attached to a ship near the origin O.

The target scatterer re-radiates the incident electric and magnetic fields, which are received by the dipole antennas. The calculation of the field scattered by the target can be a complicated problem depending on the size, shape, and composition of the target. However, if the scattering target is small compared to a wavelength, it can be modeled as a radiating electric and/or magnetic dipole with strength proportional to the incident fields. The scattered electric field at the antennas is

$$\mathbf{E}_s = \frac{k^2 e^{ikR_S}}{R_S}\left[\hat{\mathbf{R}}_S \times \left(\mathbf{m} - \hat{\mathbf{R}}_S \times \mathbf{p}\right)\right] , \tag{2}$$

where $\mathbf{m}$ and $\mathbf{p}$ are the induced magnetic and electric dipole moments:

$$\mathbf{m} = \frac{a^3}{\epsilon_0 c}\mathbf{D}^h \cdot \mathbf{H}_i , \qquad \mathbf{p} = a^3 \mathbf{D}^e \cdot \mathbf{E}_i . \tag{3}$$

$\mathbf{D}^h$ and $\mathbf{D}^e$ are the magnetic and electric polarizability tensors, which depend on the shape and composition of the target scatterer. The a^3 factor nominally accounts for the size (volume) of the scatterer. The scattered field at the antennas induces voltages $V_H = -\mathbf{d}_H \cdot \mathbf{E}_S$ and $V_V = -\mathbf{d}_V \cdot \mathbf{E}_S$ in the dipoles. If we assume the antenna dipoles have equal length d then $\mathbf{d}_H = d\,\hat{\mathbf{e}}_H$, $\mathbf{d}_V = d\,\hat{\mathbf{e}}_V$, and we can write the matrix equation

$$\begin{bmatrix} V_H \\ V_V \end{bmatrix} = -\frac{i(ka)^3}{4\pi\epsilon_0 c}\left(\frac{d}{R_S}\right)^2 e^{2ikR_S} \begin{bmatrix} K_{HH} & K_{HV} \\ K_{VH} & K_{VV} \end{bmatrix} \begin{bmatrix} I_H \\ I_V \end{bmatrix} \tag{4}$$

that relates the received voltages to the transmitting currents for each dipole. Let $\mathbf{V} = [V_H\ V_V]^T$ and $\mathbf{I} = [I_H\ I_V]^T$ ($()^T$ is the matrix transpose), then we can write (4) as

$$\mathbf{V} = -\frac{i(ka)^3}{4\pi\epsilon_0 c}\left(\frac{d}{R_S}\right)^2 e^{2ikR_S}\mathbf{K}\,\mathbf{I} . \tag{5}$$

This is the basic equation evaluated by the ISAR simulator to calculate the antenna voltages induced by the field reflected from a single point-like scatterer. For a cloud of scatterers, we sum the individual contributions from each scatterer.

The matrix elements of $\mathbf{K}$ are easier to express if we replace the cross products in equations (1) and (2) with matrix multiplications. Let $\mathbf{b} = \hat{\mathbf{R}}_S \times \mathbf{a}$. We can write this as a matrix multiplication $\mathbf{b} = \boldsymbol{\Omega}_S \mathbf{a}$, where

$$\boldsymbol{\Omega}_S = \begin{bmatrix} 0 & -\hat{R}_{Sz} & \hat{R}_{Sy} \\ \hat{R}_{Sz} & 0 & -\hat{R}_{Sx} \\ -\hat{R}_{Sy} & \hat{R}_{Sx} & 0 \end{bmatrix} . \tag{6}$$

The matrix $\mathbf{K}$ can then be written

$$\mathbf{K} = \begin{bmatrix} \hat{\mathbf{e}}_H^T \, \mathbf{G} \, \hat{\mathbf{e}}_H & \hat{\mathbf{e}}_H^T \, \mathbf{G} \, \hat{\mathbf{e}}_V \\ \\ \hat{\mathbf{e}}_V^T \, \mathbf{G} \, \hat{\mathbf{e}}_H & \hat{\mathbf{e}}_V^T \, \mathbf{G} \, \hat{\mathbf{e}}_V \end{bmatrix} , \tag{7}$$

where $\mathbf{G} = \boldsymbol{\Omega}_S(\mathbf{D}^h + \boldsymbol{\Omega}_S \mathbf{D}^e \boldsymbol{\Omega}_S)\boldsymbol{\Omega}_S$, and $\hat{\mathbf{e}}_{H,V}$ are considered 3×1 column vectors.

The shape and composition of the scatterer determines the values of the polarization tensors. For a perfectly conducting sphere, the tensors have the simple form

$$\mathbf{D}^h = -\frac{1}{2}\mathcal{I} , \quad \mathbf{D}^e = \mathcal{I} , \tag{8}$$

where $\mathcal{I}$ is the identity tensor. The size parameter a is the radius of the sphere. The tensors for a perfectly conducting wire segment of length L and thickness W are

$$\mathbf{D}^h = 0 , \quad \mathbf{D}^e = \frac{1}{3}\hat{\mathbf{b}} \otimes \hat{\mathbf{b}} , \tag{9}$$

where $\hat{\mathbf{b}}$ is the unit vector along the axis of the wire and $\otimes$ is the outer product. The size parameter a can be derived from

$$a^3 = \frac{L^3}{8 \ln(L/W)} . \tag{10}$$

These expressions are to leading order in W/L. Perhaps more interesting are the tensors for a perfectly conducting disk of radius a and thickness W (to leading order in a/W):

$$\mathbf{D}^h = \frac{2}{3\pi}\hat{\mathbf{b}}_3 \otimes \hat{\mathbf{b}}_3 , \quad \mathbf{D}^e = \frac{4}{3\pi}\left(\hat{\mathbf{b}}_1 \otimes \hat{\mathbf{b}}_1 + \hat{\mathbf{b}}_2 \otimes \hat{\mathbf{b}}_2\right) , \tag{11}$$

where $\hat{\mathbf{b}}_3$ is the unit vector for the axis of the disk (perpendicular to the plane of the disk), and $\hat{\mathbf{b}}_1$ and $\hat{\mathbf{b}}_2$ are two orthogonal unit vectors within the plane of the disk. Similar expressions exist for other common shapes composed of perfectly conducting or dielectric material. In the most general case, the object can be described by six degrees of freedom, three for the magnetic polarizability and three for the electric polarizability.

These scatterers are features on a ship which is moving on a set course and rotating in response to wave motion. The scatterer position vector $\mathbf{r}$ is broken down into a component due to course and a local component that specifies the relation between the scatterer and the ship center. In addition, the polarization tensors are more conveniently described in a coordinate system fixed to the ship. However, these must be transformed to the earth-based system to correctly calculate the response to the illuminating radiation. Let $\mathbf{r}_s(t)$ be the position of the center of the ship at time t from the origin O in Fig. 1, and $\boldsymbol{\rho}$ the position of the scatterer relative to the ship center. Furthermore, let $\psi(t)$, $\theta(t)$, and $\phi(t)$ be the roll, pitch, and yaw angles respectively at time t for the ship. The transformation between the ship-based coordinate system to the earth-based coordinate system involves a translation specified by $\mathbf{r}_s(t)$ and the general rotation specified by ψ,θ, and ϕ. The rotational part is described by three orthogonal matrices:

$$\mathbf{R}_y(\phi) = \begin{bmatrix} \cos\phi & 0 & \sin\phi \\ 0 & 1 & 0 \\ -\sin\phi & 0 & \cos\phi \end{bmatrix} , \quad \mathbf{R}_p(\theta) = \begin{bmatrix} \cos\theta & -\sin\theta & 0 \\ \sin\theta & \cos\theta & 0 \\ 0 & 0 & 1 \end{bmatrix} , \quad \mathbf{R}_r(\psi) = \begin{bmatrix} 1 & 0 & 0 \\ 0 & \cos\psi & -\sin\psi \\ 0 & \sin\psi & \cos\psi \end{bmatrix} . \tag{12}$$

These are combined to describe the overall rotation between the ship coordinate system and the earth coordinate system:

$$\mathbf{R}_{es}(\phi,\theta,\psi) = \mathbf{R}_y(\phi)\mathbf{R}_p(\theta)\mathbf{R}_r(\psi)\ . \tag{13}$$

The scatterer location at time t is then

$$\mathbf{r}(t) = \mathbf{r}_s(t) + \mathbf{R}_{es}\left(\phi(t),\theta(t),\psi(t)\right)\,\boldsymbol{\rho}\ . \tag{14}$$

Given the polarization tensors $\mathbf{D}_s^e$ and $\mathbf{D}_s^h$ in the ship coordinate system, the tensors in the earth coordinate systems are

$$\mathbf{D}^h = \mathbf{R}_{es}\,\mathbf{D}_s^h\,\mathbf{R}_{es}^T\ , \quad \mathbf{D}^e = \mathbf{R}_{es}\,\mathbf{D}_s^e\,\mathbf{R}_{es}^T\ . \tag{15}$$

The final expression for the $\mathbf{G}$ tensor used to calculate $\mathbf{K}$ in equation (7) is

$$\mathbf{G} = \boldsymbol{\Omega}_S\,\left(\mathbf{R}_{es}\,\mathbf{D}_s^h\mathbf{R}_{es}^T + \boldsymbol{\Omega}_S\,\mathbf{R}_{es}\,\mathbf{D}_s^e\,\mathbf{R}_{es}^T\,\boldsymbol{\Omega}_S\right)\boldsymbol{\Omega}_S\ . \tag{16}$$

This is a function of time t since both the rotation tensor and the unit vector $\hat{\mathbf{R}}_s$ that specifies $\boldsymbol{\Omega}_S$ change with time.

At this point we can describe the overall algorithm for calculating the polarimetric radar return from a moving ship. The ship is modeled as a collection of individual scattering points whose shape, size, and position on the ship are known. In addition, the course, roll, pitch, and yaw of the ship are specified as functions of time. At any time instant t, the position of each scatterer is calculated using equation (14), which also requires the rotation tensor (13) at time t. This is then used to calculate $\mathbf{G}$ (eq. (16)), $\mathbf{K}$ (eq. (7)), and finally the voltages using equation (5). Summing the contributions from all the scatterers on the ship gives the overall response at time t. The process is repeated for later times after updating the ship course and rotation angles.

In addition to reflection from a target vessel, a radar looking at the ocean receives a large number of reflections from various features of the ocean wave field. These include edge diffraction from wave crests, Bragg scattering from smaller scale surface roughness, and possible specular reflections from the large waves themselves. These collective effects, called clutter, create a randomly varying background in ISAR images of the ocean. The simulation of the radar return from these features would be exceedingly complicated given the variety of physical mechanisms that scatter radar and the uncertainty in the characterization of the ocean surface. Rather than attempt such a detailed simulation, we have two possible ways to model surface clutter: statistical models in the image domain, or simplified scattering models for the surface. Statistical models attempt to characterize the image clutter in terms of distributions for pixel intensities and correlations between pixels. A realization of image clutter can be obtained in principle by sampling from these distributions and adding it to the ISAR image of the target alone. We would expect the pixel clutter distributions to depend on the environmental conditions and radar parameters. This approach to clutter modeling should be investigated since it is based on empirical models from actual data. However, it would take time to research the variety of models and select ones to implement.

An alternative to image clutter models is to create background radar returns from random distributions of point-like scatterers over the ground plane corresponding to the ocean surface. We use this approach in the initial version of the ISAR simulator. We model the clutter scatterers as perfectly conducting spheres with a specified diameter and areal density on the ground surface. A clutter area is selected around the target and the spheres are distributed uniformly over the area at a specified average areal density. The sum of the returns from the individual spheres is added to the simulated target data. Currently, the scatterers are assume to persist unchanged over the total illumination time of the radar. However, radar platform motion gives the clutter an apparent movement during the illumination time making the modeled clutter returns change with time. The calculation of the return for each sphere is identical to the calculation for each scattering point from the target (eq. (4)). Thus the total radar return for a specific frequency f at time t can be expressed as a sum over N_S target scattering points plus a sum over N_C clutter scattering points:

$$\mathbf{V}(f,t) = \sum_{j=1}^{N_S}\mathbf{V}_j^S + \sum_{l=1}^{N_C}\mathbf{V}_l^C\ , \tag{17}$$

where $\mathbf{V}_j^S(f,t)$ is the return from the *jth* target scattering point, and $\mathbf{V}_l^S(f,t)$ is the return from the *lth* clutter point. These differ in their size a, distance $R_S(t)$, and matrix $\mathbf{K}(f,t)$. We have added the frequency and time dependence to indicate the frequency dependence of the scattering amplitude and time dependence of the geometry for a moving target.

The final step in simulating ISAR data is to incorporate the actual operation of the radar into the calculation of the radar returns. For example, a stepped frequency radar emits a sequence of $N+1$ single-frequency pulses starting with frequency f_0 and ending at frequency $f_0 + N\Delta f$, i.e. $f_n = f_0 + n\Delta f$: $n = 0, 1, ..., N$. Each pulse is emitted at time $t_n = t_0 + n\Delta t$, $n = 0, 1, ..., N$, where $1/\Delta t$ is the pulse repetition frequency (PRF). Each sequence is called a *burst*, and is repeated at regular intervals of Δt_b. Thus the *nth* pulse from the *mth* burst occurs at time $t_{mn} = t_0 + n\Delta t + m\Delta t_b$ $(m = 0, 1, ..., M)$, with the constraint $\Delta t_b > N\Delta t$. The corresponding radar returns are

$$\mathbf{V}_{mn} = \mathbf{V}(f_n, t_{mn}) \, . \tag{18}$$

A typical ISAR radar might have a starting frequency of 9 GHz ($f_0 = 9 \times 10^9$), bandwidth of 100 MHz, with 128 pulses in a burst ($N = 128$) at a pulse repetition frequency of 40 kHz ($\Delta t = 25\,\mu s$).

3 ISAR reconstruction

The goal of ISAR is to transform a sequence of received radar pulses into an image of the object in the field of view. In the previous section we presented a physical model of the radar scattering process describing how the transmitted radar pulses are reflected from an object. The ISAR reconstruction process unravels the information about the object that is encoded in the radar returns. This process is typically derived for a two dimensional geometry (Fig. 2) even though the application space is three dimensional [1]. In this note we will present the reconstruction process in two dimensions, leaving the three-dimensional case to a later report.

The imaging geometry for ISAR reconstruction is shown in Figure 2. The target is described by a set of scattering points P with coordinates (x, y) in the system attached to the target. This system is rotated from the radar coordinate system (X, Y) by an angle $\theta(t)$. The standoff distance (range) to the target center is $R(t)$. Both R and θ change with time as the target moves relative to the radar:

$$R(t) = R_0 + vt + \frac{1}{2}at^2 \, , \tag{19}$$

$$\theta(t) = \theta_0 + \Omega t + \frac{1}{2}\alpha t^2 \, , \tag{20}$$

where v and a are the target velocity and acceleration in the range direction. Ω and α are the rotational velocity and acceleration of the target. The velocities and accelerations are assumed to be constant over the time the radar takes to acquire an imaging data set (dwell time). The relationship between the coordinates of a scattering point P in the target reference frame and the coordinates in the radar frame is

$$X = x\cos\theta(t) - y\sin\theta(t) \, , \tag{21}$$

$$Y = x\sin\theta(t) + y\cos\theta(t) \, . \tag{22}$$

For $R(t) >> L$, the range from the radar to the scattering point is $r(t) \simeq R(t) + Y$, *i.e.*

$$r(t) \simeq R(t) + x\sin\theta(t) + y\cos\theta(t) \, . \tag{23}$$

Let the radar emit a single frequency pulse with amplitude $A(\omega)$ and angular frequency ω, then we can write the reflected signal for a single polarization component as [1]

$$V(\omega, t) = A(\omega) \iint q(x,y) e^{i[\omega t - 2kr(t)]} \, dx \, dy \, , \tag{24}$$

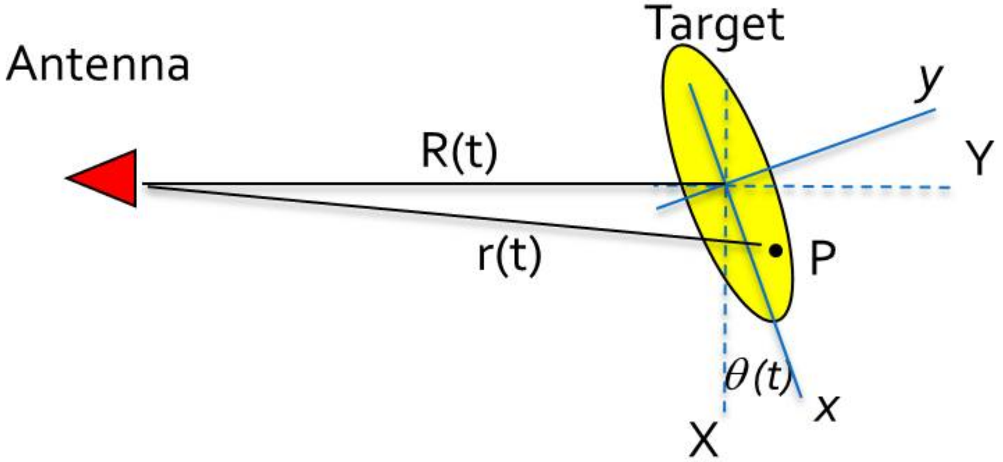

Figure 2: Imaging geometry for two-dimensional ISAR reconstruction. The lower case (x, y) denote the coordinate system attached to the target, which is rotated an angle θ from the fixed radar coordinate system (X, Y). Both the rotation angle and the standoff distance R are functions of time t. The distance from the radar to a specific scattering point P on the target from is $r(t)$. The standoff distance is assumed to be much greater than the characteristic size L of the target, $R(t) >> L$.

where $k = \omega/c$, c is the speed of light, and $q(x, y)$ is the distribution of scatterers in the target. The range of integration is implied to be over the target. In typical stepped frequency radar, the duration of each pulse T_p is small compared to the time between pulses ($T_p << \Delta t$). During the pulse, we can neglect any target movement so that $r(t)$ is constant. The return signal for the *nth* pulse of the *mth* burst can be written

$$V_{mn}(t) = A_n e^{i\omega_n t} \iint q(x,y) e^{-2ik_n r(t_{mn})}\, dx\, dy\,, \quad \omega_n = 2\pi f_n\,. \tag{25}$$

If we apply base-banding we obtain

$$\begin{aligned} V_{mn} &= \frac{1}{T_p}\int_0^{T_p} V_{mn}(t) e^{-i\omega_n t}\, dt \\ &= A_n \iint q(x,y) e^{-2ik_n r(t_{mn})}\, dx\, dy\,. \end{aligned} \tag{26}$$

Substituting equation (23) for $r(t)$ gives

$$V_{mn} = A_n e^{-2ik_n R(t_{mn})} \iint q(x,y) e^{-2ik_n [x \sin\theta(t_{mn}) + y\cos\theta(t_{mn})]}\, dx\, dy\,. \tag{27}$$

During the dwell time, the radar emits a sequence of M bursts, each with N pulses, for a total duration of $M\Delta t_b$. Assuming we can neglect the target's angular acceleration over that time and that $M\Delta t_b\Omega << 1$, then we have

$$\sin\theta(t_{mn}) \simeq \sin\theta_0 + \Omega t_{mn}\cos\theta_0\,, \tag{28}$$

$$\cos\theta(t_{mn}) \simeq \cos\theta_0 - \Omega t_{mn}\sin\theta_0\,. \tag{29}$$

Thus

$$x \sin\theta(t_{mn}) + y\cos\theta(t_{mn}) \simeq Y_0 + \Omega t_{mn} X_0 \, , \tag{30}$$

where $Y_0 = x\sin\theta_0 + y\cos\theta_0$ and $X_0 = x\cos\theta_0 - y\sin\theta_0$. We can now express the received pulse amplitude V_{mn} as

$$\begin{aligned} V_{mn} &\simeq A_n e^{-2ik_n R(t_{mn})} \iint q(X_0, Y_0) e^{-2ik_n(Y_0 + \Omega t_{mn} X_0)} \, dX_0, dY_0 \\ &\simeq 4\pi^2 A_n e^{-2ik_n R(t_{mn})} Q(2k_n \Omega t_{mn}, 2k_n) \, , \end{aligned} \tag{31}$$

where $Q(\kappa_x, \kappa_y)$ is the two-dimensional spatial Fourier transform of $q(x, y)$:

$$Q(\kappa_x, \kappa_y) = \frac{1}{4\pi^2} \iint q(x, y) e^{-i(\kappa_x x + \kappa_y y)} \, dx \, dy \, . \tag{32}$$

The inverse transform is

$$q(x, y) = \iint Q(\kappa_x, \kappa_y) e^{i(\kappa_x x + \kappa_y y)} \, d\kappa_x \, d\kappa_y \, . \tag{33}$$

Equation (31) is the principle result of this section. It shows that the sequence of base-banded returns (V_{mn}) sample the 2D spatial Fourier transform of the target scattering distribution $Q(\kappa_x, \kappa_y)$. The purpose of the reconstruction algorithm is to remove the prefactors and perform the inverse Fourier transform to recover the target distribution $q(x, y)$. The prefactors are of two types: the transmitted pulse amplitudes A_n which should known and can be eliminated through calibration, and the phase factor (complex exponential) which is generated by the variation in range of the target over the dwell time. The estimation and removal of the range variation factor is called *coarse motion compensation* and there are multiple algorithms that can be used [1]. Once these prefactors are removed we can write the remaining part as

$$\hat{Q}_{mn} = Q(2k_n \Omega t_{mn}, 2k_n) \, . \tag{34}$$

The second argument of Q samples the Fourier variable κ_y which is the range direction in physical space. The first argument samples κ_x, the cross-range variable, non-uniformly. The target rotational velocity Ω is usually not known, making the cross-range scaling uncertain. This argument can be interpreted as the Doppler shift of the frequency pulses due to the target's rotation. Since the tangential velocity of each scatterer in the target is proportional to its distance from the rotation axis, the Doppler shift can be used to resolve its cross-range position. The primary difficulty in inverting eqn. (34) is the sampling in the Fourier spatial frequency domain. In particular, the sampling in κ_x depends in both indices m and n. In fact k_n appears explicitly as a factor in the κ_x argument. Expanding this argument explicitly using the definitions of k_n and t_{mn} for a stepped frequency radar gives

$$2\Omega k_n t_{mn} = \frac{4\pi\Omega}{c} \left[f_0 t_0 + n(\Delta f t_0 + f_0 \Delta t) + m f_0 \Delta t_b + mn \Delta f \Delta t_b + n^2 \Delta f \Delta t \right] \, . \tag{35}$$

Choosing the time origin to be the beginning of the pulse sequence ($t_0 = 0$) simplifies this to

$$\begin{aligned} 2\Omega k_n t_{mn} &= \frac{4\pi\Omega f_0}{c} \left[n\Delta t + m\Delta t_b + \frac{\Delta f}{f_0} \left(mn\Delta t_b + n^2 \Delta t \right) \right] \\ &= \frac{4\pi\Omega f_0}{c} \left(n\Delta t + m\Delta t_b \right) \left(1 + n\frac{\Delta f}{f_0} \right) \, . \end{aligned} \tag{36}$$

For reference the κ_y sampling is given by

$$2k_n = \frac{4\pi f_0}{c} \left(1 + n\frac{\Delta f}{f_0} \right) \, . \tag{37}$$

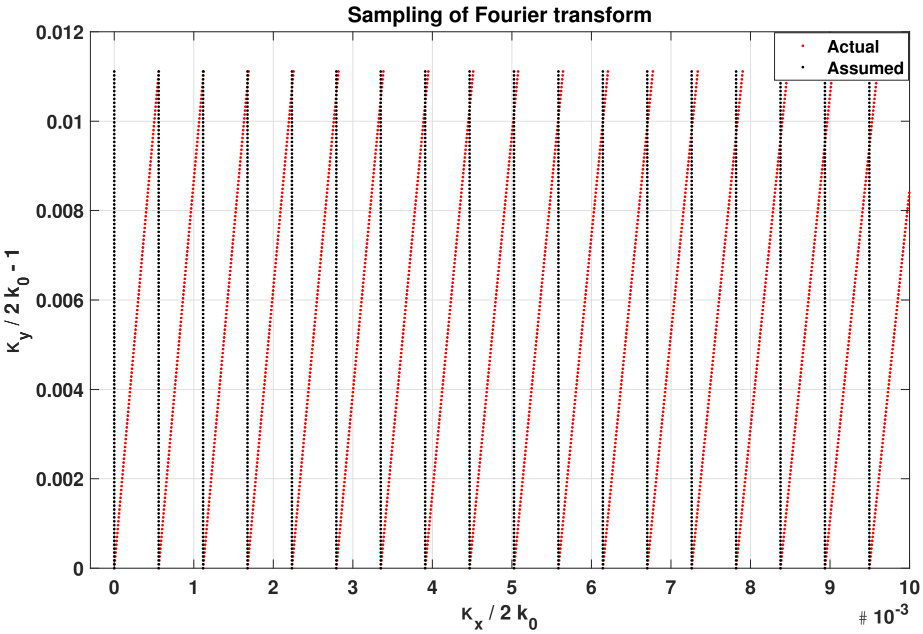

Figure 3: Sampling of the spatial Fourier transform for a typical ISAR radar (see text). The red dots are the true samples based on equations (36) and (37). The black dots is the uniform sampling assumed by the conventional inverse FFT method [1]. Note the change in initial slope of the lines of true sample points as κ_x increases.

As n increases from 0 to N, keeping m fixed, the κ_x argument increases, defining a curve in the $\kappa_x - \kappa_y$ plane. Since the highest power is n^2, the curve is quadratic. As m varies the sampling defines a sequence of quadratic curves, each starting at $\kappa_x = 4\pi\Omega f_0 t_0 m\Delta t_b/c$, $\kappa_y = 4\pi f_0/c$ with different initial slopes. Figure 3 shows the sampling in the spatial Fourier space specified by equation (36) for the specific case of $\Omega = 10\,\mathrm{deg}/s$, $\Delta t = 25\,\mu s$, $N = 128$, and $\Delta f/f_0 = 0.0111$. The red dots are the true samples and the black dots show the sampling assumed by the conventional inverse FFT imaging method [1]. Note that the initial slopes of the true sampling curves change with increasing κ_x. The curvature of the sample curves is imperceptible on this scale since the quadratic term in (36) is very small.

The conventional ISAR reconstruction technique [1] ignores the true sampling and assumes the samples are arranged on a uniform grid whose grid lines are parallel to the κ_x and κ_y axes. The final step is then to perform a two-dimensional inverse Fast Fourier Transform (iFFT) to create an image of the target object. Since the target rotation rate is usually unknown, the cross-range (x) scale is ambiguous. We can calculate the result analytically by applying the inverse Discrete Fourier Transform (iDFT):

$$\hat{q}(x, y) = \sum_{m=-M/2}^{M/2} \sum_{n=-N/2}^{N/2} \hat{Q}_{mn} e^{2\pi i(mx/L_x + ny/L_y)}\,, \tag{38}$$

where we have shifted the summation indices for convenience. Both the iFFT and iDFT create images that are periodic in x and y with periods L_x and L_y respectively. In practice, only one period of the image is required. Combining the definitions of $Q(\kappa_x, \kappa_y)$ (eq. (32)) and $\hat{Q}_{mn}$ (eq. (34)) and interchanging the integration and the summation gives

$$\hat{q}(x, y) = \frac{1}{4\pi^2} \int\int dx'\, dy'\, q(x', y') \sum_{m=-M/2}^{M/2} \sum_{n=-N/2}^{N/2} e^{2i\left(\pi mx/L_x - \Omega k_n t_{mn} x'\right)} e^{2i\left(\pi ny/L_y - k_n y'\right)}\,. \tag{39}$$

This has the form of a convolution between the true target scattering distribution $q(x', y')$ and an imaging point spread function (PSF) $h(x, y; x', y')$ represented by the double summation. The PSF describes the blurring created by the imaging system. The ideal PSF would be $h(x, y; x', y') = \alpha\delta(x - x')\delta(y - y')$ so that $\hat{q}(x, y) = \alpha q(x, y)$, *i. e.* the image is a scaled version of the target. However, this is never attained in practice due to the finite wavelength of the radiation and limited aperture of the imaging system. One way to assess the quality of the imaging system is to measure how well the PSF approximates the ideal given the wavelength and aperture constraints. Note that the double summation cannot be factored into the product of two summations due to the t_{mn} term in the first exponential.

If the fractional bandwidth of the radar is small ($N\Delta f/f_0 \ll 1$), then

$$2\Omega k_n t_{mn} \simeq \frac{4\pi\Omega f_0}{c} \left(n\Delta t + m\Delta t_b\right) . \tag{40}$$

Furthermore, since $\Delta t_b \geq N\Delta t$ we have

$$\left(m - \frac{1}{2}\right) \Delta t_b \leq (n\Delta t + m\Delta t_b) \leq \left(m + \frac{1}{2}\right) \Delta t_b . \tag{41}$$

This means the effect of the $n\Delta t$ term is small compared to $m\Delta t_b$ except for the lowest order terms of the sum over m ($|m| \lesssim 10$). Another interpretation is that if the 2D Fourier transform $Q(\kappa_x, \kappa_y)$ is slowly varying over spatial frequency scales $\Delta\kappa_x = 4\pi\Omega f_0 \Delta t_b/c$, then we can ignore the variation of eq. (36) over the summation index n and write

$$2\Omega k_n t_{mn} \simeq \frac{4\pi\Omega f_0}{c} m\Delta t_b . \tag{42}$$

This is the approximation assumed in conventional ISAR reconstruction [1], which reduces the final inversion step (eq. (38)) to an inverse FFT. Here we show explicitly the approximations that lead to the iFFT method, and are not often discussed in presentations of ISAR reconstruction.

Neglecting the n^2 term in eq. (36) and using the identity

$$\sum_{n=-N/2}^{N/2} e^{2\pi i n a} = \frac{\sin\left[(N+1)\pi a\right]}{\sin(\pi a)} , \tag{43}$$

we can perform the sum over n to obtain

$$h(x, y; x', y') = e^{-4\pi i f_0 y'/c} \sum_{m=-M/2}^{M/2} \frac{\sin\left[(N+1)\pi a_m(y; x', y')\right]}{\sin\left[\pi a_m(y; x', y')\right]} e^{2\pi i m\left(x/L_x - 2\Omega f_0 \Delta t_b x'/c\right)} , \tag{44}$$

where

$$a_m(y; x', y') = \frac{y}{L_y} - \frac{2\Delta f y'}{c} - \frac{2\Omega f_0 \Delta t x'}{c} \left(1 + \frac{\Delta f}{f_0} \frac{\Delta t_b}{\Delta t} m\right) . \tag{45}$$

If we assume $\Delta t_b/\Delta t \simeq N$, then

$$\frac{\Delta f}{f_0} \frac{\Delta t_b}{\Delta t} m \simeq \frac{N\Delta f}{f_0} m \leq \frac{N\Delta f}{f_0} \frac{M}{2} . \tag{46}$$

By limiting the number of bursts M to be much smaller than the reciprocal of the bandwidth, we can neglect the m term in a_m ($a_m \simeq a_0$) and use (43) to evaluate the sum over m to obtain

$$h(x, y; x', y') = \frac{\sin\left[(N+1)\pi a_0(y; x', y')\right]}{\sin\left[\pi a_0(y; x', y')\right]} \frac{\sin\left[(M+1)\pi b(x; x')\right]}{\sin\left[\pi b(x; x')\right]} e^{-4\pi i f_0 y'/c} , \tag{47}$$

with

$$b(x; x') = \frac{x}{L_x} - \frac{2\Omega f_0 \Delta t_b x'}{c} . \tag{48}$$

This is equivalent to sampling the spatial Fourier transform along the black dots in Fig. 3.

Up to this point we have not specified the lengths L_x and L_y of the imaging domain. For discretely sampled Fourier transforms, the lengths are related to the fine scale of the sampling, *i.e.* $L_y = 2\pi/\Delta\kappa_y$, $L_x = 2\pi/\Delta\kappa_x$. For κ_y we can write

$$\Delta\kappa_y = 2\left(k_{n+1} - k_n\right) = \frac{4\pi\Delta f}{c}\ , \tag{49}$$

so that

$$L_y = \frac{c}{2\Delta f}\ . \tag{50}$$

Proceeding similarly for κ_x gives

$$\Delta\kappa_x = 2\Omega k_n\left(t_{m+1,n} - t_{mn}\right) = \frac{4\pi\Omega f_0\Delta t_b}{c}\left(1 + \frac{n\Delta t}{f_0}\right)\ . \tag{51}$$

In this case the choice for L_x is somewhat ambiguous since $\Delta\kappa_x$ depends on n, the index for κ_y. If the fractional bandwidth of the radar is small, this variation can be neglected ($n = 0$) so we obtain

$$L_x = \frac{c}{2\Omega f_0\Delta t_b}\ . \tag{52}$$

Given these expressions for L_x and L_y, a_m and b become

$$\begin{aligned} a_m(y;x',y') &= \frac{y-y'}{L_y} - \frac{\Delta t}{\Delta t_b}\frac{x'}{L_x}\left(1 + \frac{\Delta f}{f_0}\frac{\Delta t_b}{\Delta t}m\right) \\ &\simeq \frac{y-y'}{L_y} - \frac{x'}{NL_x}\left(1 + \frac{N\Delta f}{f_0}m\right)\ , \qquad (53) \\ b(x;x') &= \frac{x-x'}{L_x}\ . \qquad (54) \end{aligned}$$

This defines the periodicity of the PSF and the resulting image $\hat{q}(x,y)$. Note that L_y is determined only by the radar parameters while L_x requires knowledge of the object rotation rate Ω. Since the number of samples in y is N, the range resolution of the image is

$$\Delta y = \frac{L_y}{N} = \frac{c}{2N\Delta f}\ . \tag{55}$$

Thus the bandwidth $N\Delta f$ of the radar controls the range resolution, and the number of frequencies N determines the imaging domain size in the range (y) direction. The cross range (x) resolution is given by

$$\Delta x = \frac{L_x}{M} = \frac{c}{2\Omega f_0 M\Delta t_b}\ . \tag{56}$$

This can be refined by increasing either the radar center frequency f_0 or the overall dwell time $M\Delta t_b$. However, the actual cross range resolution attained by the system depends on the object rotation rate Ω, which may not be controllable. Alternatively, we can express the cross range resolution as the radar center wavelength $\lambda_0 = c/f_0$ divided by twice the angular rotation of the target ($\theta = \Omega M\Delta t_b$) during the dwell time ($\Delta x = \lambda_0/2\theta$). The greater the rotation, the better the cross range resolution. These estimates for range and cross-range resolution can be found in ISAR reference texts such as Özdemir [1].

4 Examples

To illustrate the generation and reconstruction of polarimetric ISAR data, we consider a simulated test object consisting of an arrangement of small perfectly conducting rods (Fig. 4). The arrangement and direction

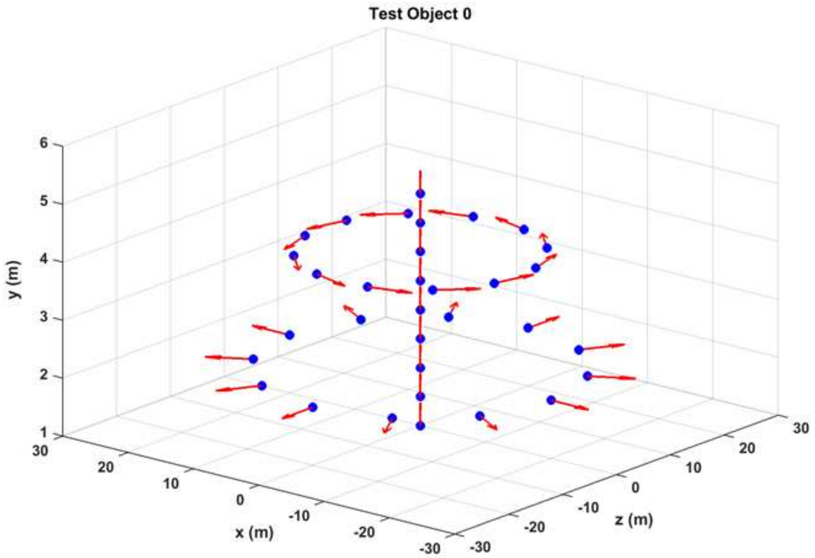

Figure 4: Test object consisting of two circles of twelve perfectly conducting thin rods and a central line of nine rods. The rod directions are chosen to illustrate the responses to different radar polarization components. Each rod is nominally 10 cm long.

were chosen to show the variation of object visibility with radar polarization. The electric field incident on each rod induces a current along the axis, which then radiates a dipole scattered field. Simulated data is generated for a stepped frequency radar with starting frequency of 9 GHz ($f_0 = 9 \times 10^9$) and bandwidth of 100 MHz. There are 128 pulses in each burst ($N = 128$) with a pulse repetition frequency of 40 kHz ($\Delta t = 25\, \mu s$). The antenna is a crossed dipole (element length 30 cm) and placed at a horizontal range of 5 km from the object. Two antenna altitudes are considered, 0 and 1000 meters. The 0 meter altitude is effectively a two-dimensional case where the incident electric field is in a vertical plane and some of the rods may not generate any significant returns for particular polarizations. The 1000 meter altitude is a more realistic three dimensional situation where each rod will contribute to the overall radar return for all polarizations.

Figure 5 shows ISAR reconstructions using the conventional inverse FFT algorithm of simulated scattering data from the test object in Fig. 4. Each image is created from 128 bursts as the test object rotates around the vertical (y) axis (yaw) at a rate of 5°/sec. For the upper row the antenna elevation was zero, which creates a largely two dimensional scattering problem. The circular arrangements of rods in the test object are only visible in the HH polarization since both the incident and scattered electric fields in the HH case are in the horizontal plane. Similarly, only the vertical rods are visible in VV. The HV image is zero since all the rods are either horizontal or vertical, and the scattered fields at the antenna reflect this symmetry. In the lower row, the antenna was at an elevation of 1000 meters (11.3° grazing angle). For this case, the rods int he object do not align with polarization of the incident field, producing returns from all rods for each polarization, including cross-polarization (HV). In both 2D and 3D cases, the visibility of each rod around the two circles varies accordingly to its alignment with the incident electric field vector. The response is largest when the rod axis is aligned with the field. This is particularly noticeable in the HH images.

In the previous section we showed that the sampling of the two-dimensional spatial Fourier transform of the object is non-uniform (fig. 3). The ISAR reconstructions above used the conventional approach which ignores the non-uniformity. Since the sampling is known (eqs. (36) and (37)) we can resample the data on

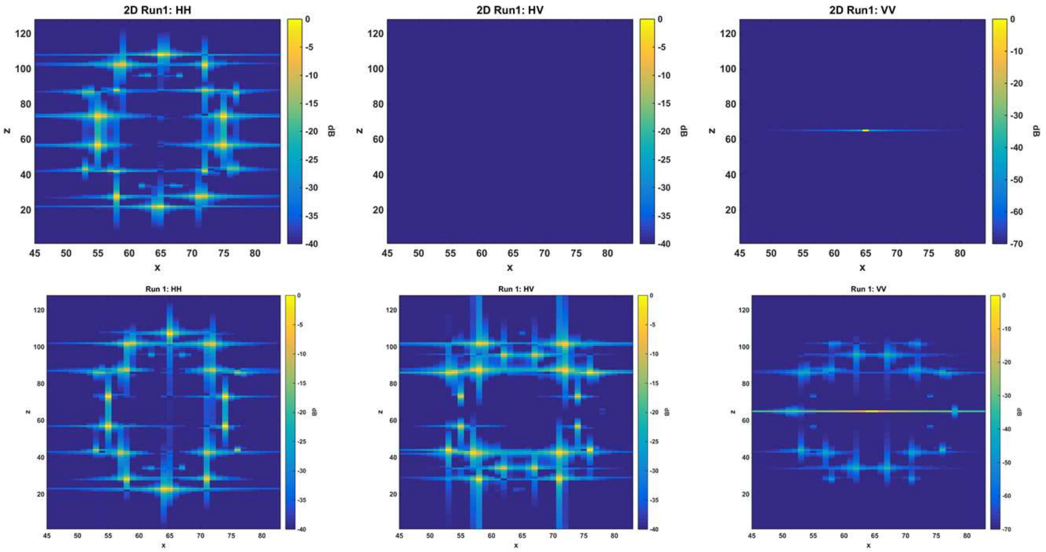

Figure 5: ISAR reconstructions of simulated data for the test object in Fig. 4. Upper row shows 2D case (zero elevation) and lower row the 3D case (1000m elevation). The columns are reconstructions for different polarization combinations (HH, HV, VV), displayed in dB.

to a uniform grid before performing the inverse FFT, eliminating distortion caused by the original sampling. Rewriting the κ_x sampling,

$$\kappa_x = 2\Omega k_n t_{mn} = \frac{4\pi\Omega f_0 \Delta t_b}{c}\left(m + \frac{n}{N}\right)\left(1 + b_f \frac{n}{N}\right) \ , \tag{57}$$

we find that the resampling depends only on the fractional bandwidth $b_f = N\Delta f/f_0$ and the number of pulses in a burst (N) when $\Delta t_b = N\Delta t$. For the test object images, the fractional bandwidth is $b_f = 1/90$. Figure 6 shows a comparison between the original images (left column) and the resampled images (right column). Only slight differences are observed since the fractional bandwidth is small and the number of pulses in a burst is large. We would expect a greater effect for wider band radars.

5 Summary

In this note we have presented described a fully polarimetric ISAR data simulator that represents the target object (*e.g.* a ship) as a collection of electrically small scatterers. We also lay out the conventional reconstruction approach for creating images from the scattering data, with careful attention to the assumptions that are used to simplify the mathematics. Finally, we show simulated polarimetric ISAR images for a test object to demonstrate the differences between polarizations and illustrate the geometric dependence on the scattering object. We also show how to correct for the non-uniform Fourier sampling of the raw data, though the correction made little difference for narrow band radars.

References

[1] Caner Özdemir, *Inverse Synthetic Aperture Radar Imaging with MATLAB® Algorithms*, John Wiley & Sons, Hoboken, New Jersey, 2012.

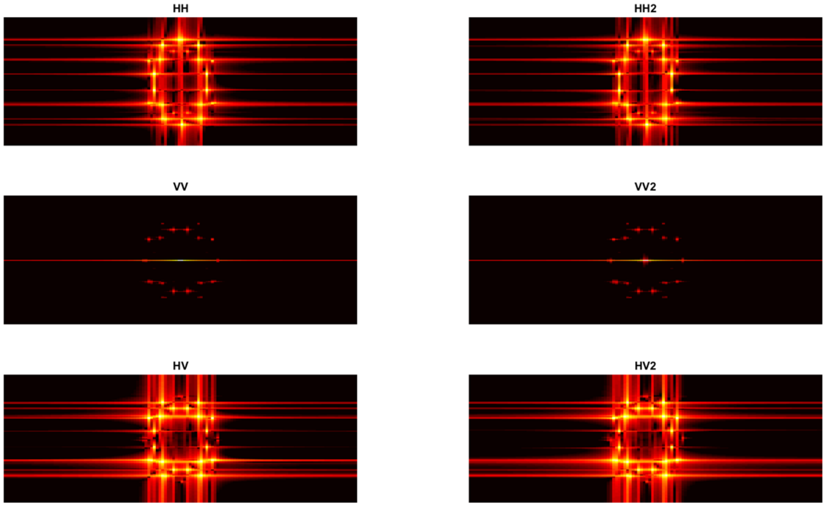

Figure 6: ISAR reconstructions of simulated data for the test object in Fig. 4. Left column shows images using the conventional inverse FFT algorithm. Right column shows images using resampled data.